Journal of
Marine Science and Engineering

MDPI

Article

Investigation of the Impact Load Characteristics during Water Entry of Airdropped Underwater Gliders

Xiangcheng Wu, Lihong Wu *, Pengyao Yu * and Xin Chang

Naval Architecture and Ocean Engineering College, Dalian Maritime University, Dalian 116026, China; xiangchengwu1993@outlook.com (X.W.); changxin_heu@outlook.com (X.C.)
* Correspondence: wlh@dlmu.edu.cn (L.W.); yupengyao@dlmu.edu.cn (P.Y.)

Abstract: Underwater gliders have emerged as effective tools for long-term ocean exploration. Employing aircraft for launching underwater gliders could significantly expand their application. Compared to slender underwater vehicles, the distinctive wing structure of underwater gliders may endure huge impact forces when entering water, leading to more intricate impact load characteristics and potential wing damage. This paper employs a computational fluid dynamics approach to analyze the water entry event of an airdropped underwater glider and its impact load behavior. The results indicate that the glider impact load is enhanced prominently by the wing, and that the extent of enhancement is influenced by the entry attitude. At an entry angle of 80°, the glider exhibits the maximum impact load during different water entry angles. In addition, a larger attack angle indicates a higher glider impact load. Our present study holds significant importance for both the hydrodynamic shape design and water entry strategy control of airdropped underwater gliders.

Keywords: airdropped underwater glider; water entry; characteristics of impact load; wing effects; computational fluid dynamics

Citation: Wu, X.; Wu, L.; Yu, P.; Chang, X. Investigation of the Impact Load Characteristics during Water Entry of Airdropped Underwater Gliders. *J. Mar. Sci. Eng.* **2024**, *12*, 808. https://doi.org/10.3390/jmse12050808

Academic Editor: Joško Parunov

Received: 6 April 2024
Revised: 6 May 2024
Accepted: 10 May 2024
Published: 13 May 2024

1. Introduction

Underwater gliders, characterized by their low energy consumption and long endurance capabilities, have found widespread application in ocean observation [1]. Launching underwater gliders to the target sea area via aircraft, as opposed to deployment by a mother ship, can significantly broaden the application scope of gliders. Nonetheless, the water entry process exposes the underwater glider to significant impact loads, which may cause damage to the glider, particularly to its wings. Therefore, research on the impact load of airdropped under9water gliders in the water entry process is essential for their application.

The investigation of water entry problems began with Von Karman's work in 1929, employing potential flow theory to calculate the impact loads on seaplane floats [2]. Wagner [3] refined Von Karman's theory by considering piled-up water surface and spray thickness effects, leading to a more precise representation. Utilizing a semi-Wagner approach, Miloh [4] achieved wetting factor computation, as well as free surface replacement with a flat equipotential surface. Korobkin and Alexander [5] incorporated higher-order terms from the Bernoulli equation into both the generalized Wagner and Logvinovich models.

The impact problems of water entry have been extensively studied using various computational fluid dynamics (CFD) techniques, as a result of computer advancements. These techniques include the arbitrary Lagrange–Euler method (ALE), the finite volume method (FVM), and the finite element method coupled with smoothed particle hydrodynamics (FEM-SPH). Based on the ALE method, Aquelet et al. [6] forecasted the high-pressure localized load exerted when a rigid wedge hits the water surface, while Wang and Soares [7] investigated the impact of elastic three-dimensional cones and hemispheres.

Based on the FEM-SPH approach, Panciroli et al. [8] investigated the hydroelastic phenomena in the water entry process of flexible wedges. Meanwhile, the FVM, a method

employed for discretizing incompressible Navier–Stokes equations, depicts the free surface of multiphase flow by incorporating the volume of fluid (VOF) technique [9]. Utilizing the FVM and VOF methods within the commercial CFD software STAR-CCM+9.06, Bilandi et al. [10] simulated the perpendicular entry of wedges into calm water at a fixed speed. Their results agree well with previously published studies. Yu et al. [11] conducted additional research concerning the entry of wedges into shallow water, quantifying the influences of ground presence on the impact force and pressure field. Wang et al. [12] investigated the impact load characteristics of water entry for various bow-flared sections. Xie et al. [13] examined the asymmetrical ship slamming loads in oblique waves.

Increasing evidence demonstrates the feasibility and efficacy of utilizing the CFD method to investigate water entry phenomena. Given the advantages of air-launched deployment, researchers have extensively investigated the water entry challenges encountered by autonomous underwater vehicles (AUVs) without wing structures. Yan et al. [14] employed high-speed photography and sensors for experimental research on the airborne-launched entry of an AUV into water, alongside numerical investigation utilizing the FEM-SPH method. The numerical outcomes, including the peak impact acceleration, align well with the experimental findings. Chaudhry et al. [15] conducted numerical simulations of the impact process when air-launched AUVs enter water, employing the ALE method, and examined how the impact loads were influenced by the velocity and angle. Shi et al. [16,17] explored the water entry challenges faced by air-launched AUVs employing the ALE method. They analyzed changes in the impact force and cavitation with varying bow shapes and water entry attitudes, as well as the influences of the bow morphology, water entry attitude and shell thickness on the structural distortion and pressure load. In addition, it takes considerable time for traditional AUVs with rotating body shapes to achieve a horizontal orientation. To shorten the distance and time required for the adjustment of the glider attitude, Wang et al. [18] examined the effect of asymmetric bow shapes on the water entry trajectory of AUVs. They also assessed how the trajectory was impacted by different water entry attitudes and bow shapes, as well as how long it took the AUV to achieve a horizontal orientation.

As reviewed above, the water entry challenges faced by air-launched AUVs have been extensively investigated. The high level of autonomy of AUVs makes them widely used in the field of marine observation [19]. Compared with AUVs, the motion mode of underwater gliders allows them to have different application scenarios. The underwater glider's long endurance enables it to meet the performance requirements for tracking and observing mesoscale eddy phenomena. For example, during an observation project on the California current system, gliders made 63 crossings of eddies over 5.5 years [20]. In addition, the motion trajectory of the underwater glider is a zigzag pattern, which enables three-dimensional sampling across mesoscale eddies, thereby analyzing the vertical structure of the eddies and observing precise seasonal changes [21].

Underwater gliders feature large wingspans. During water entry, the wings of underwater gliders may undergo substantial impact loads, possibly leading to damage to the wing structure [22]. Wings are vital for the maneuverability of underwater gliders [23]. An appropriate wing can effectively improve the motion performance of underwater vehicles [24]. Hence, despite extensive scholarly research on AUV water entry impact problems, an additional exploration of the impact characteristics of airdropped underwater gliders is warranted. However, as far as we know, comprehensive assessments on the water entry issues of airdropped underwater gliders are lacking. The present study utilizes the CFD technique to numerically investigate the water entry problem associated with airdropped underwater gliders. The impact loads experienced by the wings upon entry into water are comprehensively examined, as well as their influences on the overall glider impact load in the water entry process. Additionally, we investigate how the impact load of airdropped underwater gliders is influenced by their water entry attitude. The findings of this paper offer insights for designing the hydrodynamic shape of airdropped underwater gliders and airdrop strategies for airdropped underwater gliders.

2. Numerical Model

2.1. Airdropped Underwater Glider Model

Figure 1 illustrates the usage of three coordinate frames, i.e., the inertial O-XYZ, the body O_0-$X_0Y_0Z_0$, and the velocity V-$V_1V_2V_3$, to characterize the motion and orientation of the airdropped underwater glider. The inertial frame O-XYZ, which is stationary relative to the water surface, has OX and OY as its horizontal axes and the downward pointing OZ as its vertical axis. The body frame O_0-$X_0Y_0Z_0$ is anchored at the glider's geometric center, which is the buoyancy center after the glider completely enters the water. The distance from the origin of the body coordinate frame to the front of the bow is 532 mm. The axis $O_{0\times0}$ aligned with the longitudinal axis. Similarly, the velocity frame V-$V_1V_2V_3$ is fixed at the glider's center, with axis VV_1 aligned with the velocity vector. The water entry angle is denoted by θ, representing the angle between axis VV_1 and the water surface. α signifies the attack angle, which refers to the angle between axes O_0X_0 and VV_1; it is considered positive when $X_0O_0V_1$ rotates clockwise. In addition, this paper defines the direction of the O_0X_0 axis as the axial direction and the direction of the O_0Z_0 axis as the radial direction in the body coordinate frame.

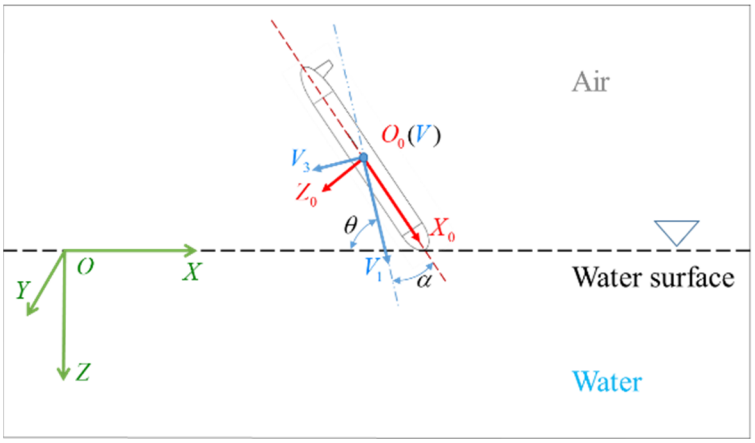

Figure 1. Coordinate frames.

Figure 2 illustrates the model of the airdropped underwater glider. The glider's main body features a Myring shape, while the wing is designed as a trapezoidal flat wing. Table 1 presents certain physical parameters of the glider. The wing position refers to the distance from the wing trailing edge to the bow tip. The gravity center denotes the coordinate of the center of gravity in the body coordinate frame.

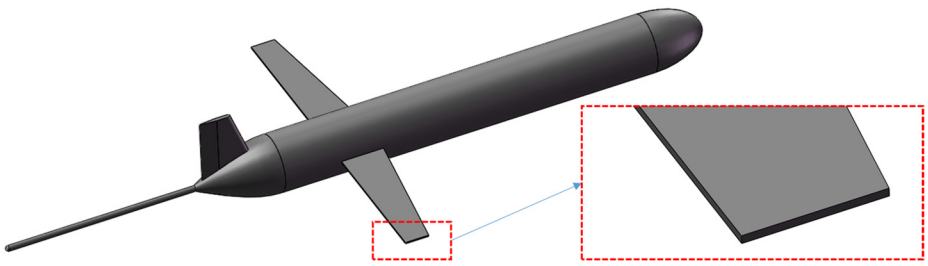

Figure 2. Airdropped underwater glider model.

Table 1. Parameters of airdropped underwater glider.

Main body parameters	bow length 120 mm	main body length 800 mm	tail length 180 mm	main body diameter 120 mm
Wing parameters	wingspan 700 mm	wing tip 50 mm	wing root 90 mm	wing position 800 mm
Glider quality	mass 11.05 kg	gravity center (0, 0, 2) mm		

2.2. Governing Equations

Both air and water are assumed to be incompressible in the numerical simulation, where temperature alterations are disregarded. Subsequently, the following continuity equation along with a Reynolds-averaged Navier–Stokes (RANS) system is formulated [25]:

$$\frac{\partial \overline{u}_i}{\partial x_i} = 0 \tag{1}$$

$$\frac{\partial(\rho\overline{u}_i)}{\partial t} + \rho\overline{u}_j\frac{\partial \overline{u}_i}{\partial x_j} = -\frac{\partial \overline{P}}{\partial x_i} + \frac{\partial}{\partial x_j}\left(\mu\frac{\partial \overline{u}_i}{\partial x_j} - \rho\overline{u_i'u_j'}\right) + \rho\overline{F}_i \tag{2}$$

where $\overline{u}_i$ is the average velocity quantities, ρ is the fluid density, $\overline{P}$ is the pressure, μ is fluid dynamic viscosity, $\rho\overline{u_i'u_j'}$ is Reynolds average stress and $\overline{F}_i$ is volume forces.

The VOF method is adopted to describe the interface between water and air. And the governing equation can be expressed as follows [26]:

$$\frac{\partial \gamma}{\partial t} + u_e \cdot \nabla\gamma = 0 \tag{3}$$

where γ is the volume fraction of water and u_e is the fluid velocity vector. $\gamma = 0$ means the grid is full of air, $\gamma = 1$ means the grid is full of water, whereas $0 < \gamma < 1$ means the grid contains both air and water. And the interface between water and air is identified by $\gamma = 0.5$.

Additionally, the RANS system is closed by utilizing the k-ε turbulence model. The structure's motion is facilitated by the Dynamic Fluid Body Interaction (DFBI) module. Physical quantity exchange between the background and overset zones is achieved using the overset mesh technique, with linear interpolation adopted at the interface. The commercial CFD software STAR-CCM+16.02 is employed to solve the governing equations in this study.

2.3. Computational Domain and Grid Configuration

Given the symmetricity of the glider about the $X_0O_0Z_0$ plane of the body coordinate system, only half the model is used in the numerical calculation to improve the calculation efficiency, as shown in Figure 3.

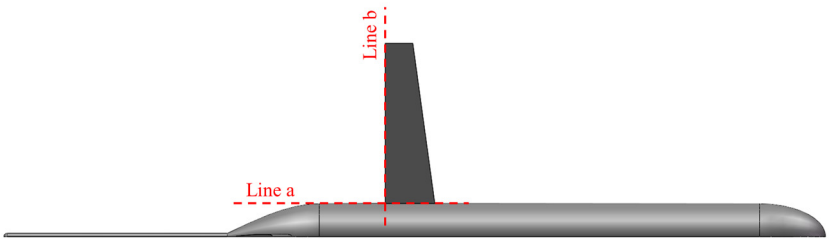

Figure 3. Numerical computational model.

As is clear from Figure 4, the computational domain is a 10.4 m long and 5.2 m wide cuboid, which is 4 m high in the air and 5.2 m deep in water. Face abcd is set as a symmetry

boundary. Faces abb'a', a'b'c'd' and dcc'd' are designated as pressure outlet boundaries, whereas faces add'a' and bcc'b' are designated as velocity inlet boundaries with velocity 0.

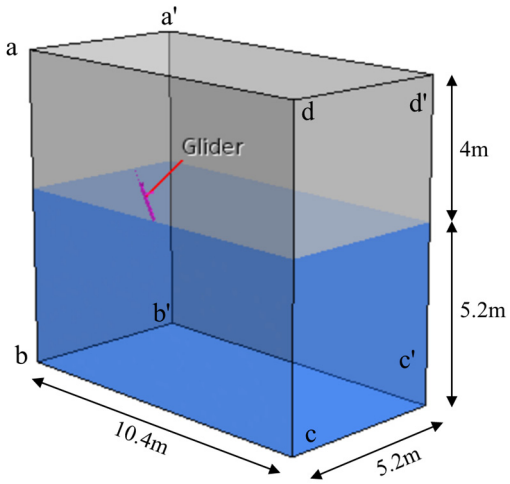

Figure 4. Computational domain.

The mesh view on the symmetry surface abcd is displayed in Figure 5. To more accurately simulate the process of glider entry into water, we densify the meshes at the air–water interface and the glider movement area.

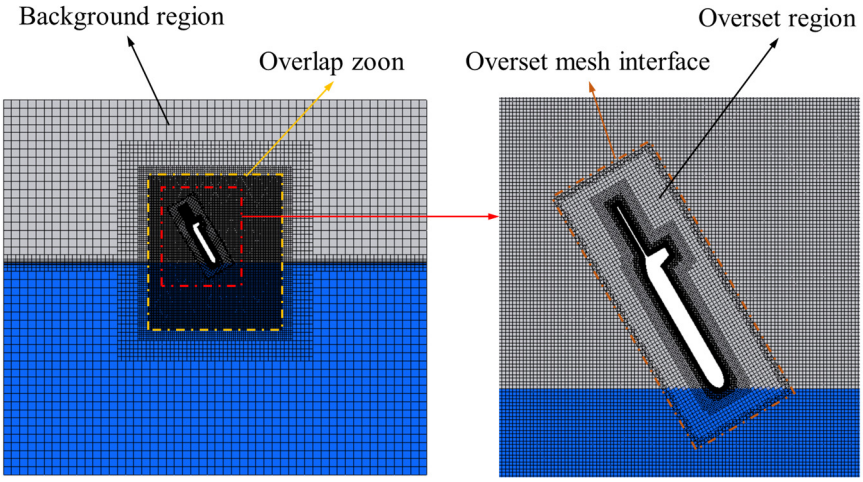

Figure 5. Mesh view on the symmetry surface abcd.

3. Discussion on the Numerical Model

3.1. Numerical Method Validation

Since experimental data on the glider's water entry impact load are lacking, this study validates the numerical simulation approach for investigating water entry problems by utilizing the classic case of a sphere entering water. The radius of the sphere is 12.7 mm and its density is 7860 kg/m^3. The water entry velocity is 2.17 m/s. In the numerical simulation, the grid strategy is the same as that in Section 2.3. Because the radius of the sphere is smaller, the minimum volume grid size is 0.125 mm in the refined zone. The prism layer mesh is assigned near the sphere to meet the non-dimensional wall distance y+ criteria. The mesh height of the first prism layer equals 0.004 mm, the number of prism layers equals 20, and the total height of the prism layer mesh is 0.56 mm. Through the above settings, it can be ensured that the y+ value is less than 5. The numerical outcomes are cross-referenced with Aristoff et al.'s experimental findings [27]. Figures 6 and 7 illustrate the comparisons of the cavity morphology and sphere displacement.

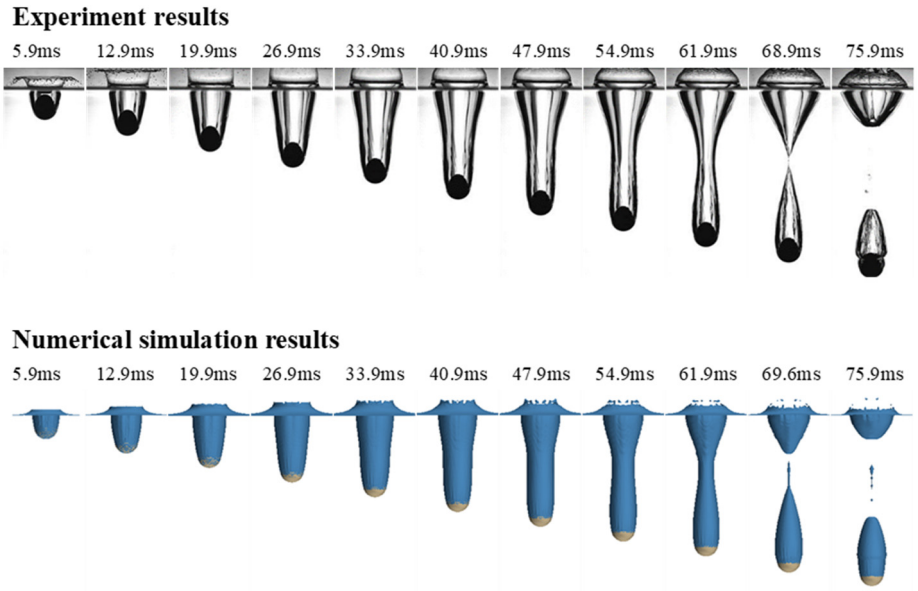

Figure 6. Comparison of water entry cavity morphology.

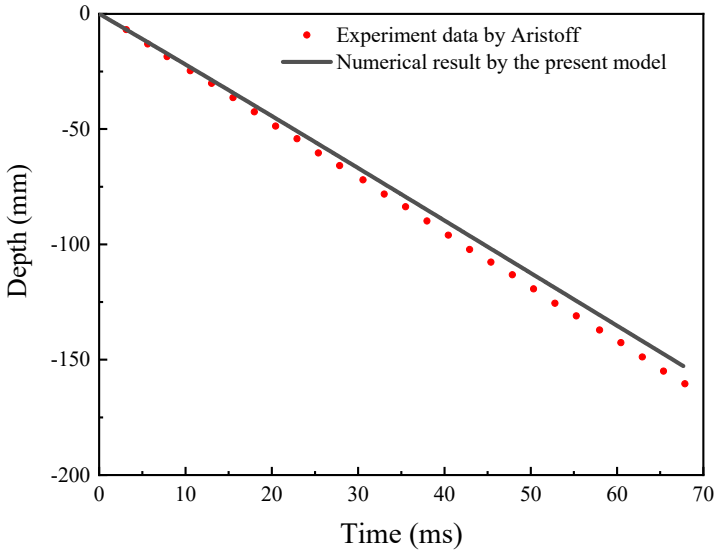

Figure 7. Comparison of the sphere displacement.

Figure 6 demonstrates that the numerical approach effectively captures the cavitation evolution process when a sphere enters water, encompassing splash formation, cavity expansion, necking, as well as cavity pitch-off. The pitch-off time is 68.9 ms in the experiment and 69.6 ms in the numerical simulation, resulting in a relative error of 1.0%. In Figure 7, at t = 65.4 ms, the sphere's displacement is 154.9 mm in the experiment and 147.6 mm in the numerical simulation, yielding a relative error of 4.7%. The simulation outcomes closely align with the experimental results, affirming the reasonableness and feasibility of the numerical method for simulating glider water entry.

3.2. Convergence Study

To ensure the reasonableness of the time-step and mesh density settings, a convergence analysis of numerical calculations is necessary. In early research, the case with glider water entry and attack angles of 90° and 0° and a water entry velocity of 10 m/s was taken as an example to discuss the convergence of the time-step and mesh density. Therefore, in the present work, another case is taken as an example to discuss the convergence of the time-step and mesh density, where the glider's water entry and attack angles are 60° and

0°, respectively, and the water entry velocity is 10 m/s. At t = 0, the distance between the glider bow and water surface is 10 mm along the glider axis.

Firstly, mesh density convergence verification is performed. The process of the glider entering water is calculated utilizing three mesh elements with different densities, which are Coarse (the number of meshes is 5,050,702), Medium (the number of meshes is 7,877,911) and Fine (the number of meshes is 12,714,652). The time-step setting is 2×10^{-5} s. Figure 8a displays the glider axial force variation with time. The axial force values obtained at various mesh densities are consistent. The Medium mesh is used in the subsequent calculations.

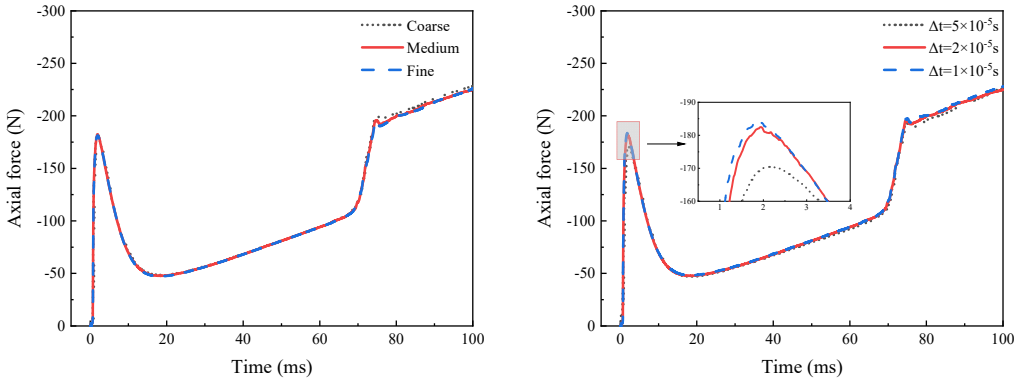

Figure 8. Mesh density and time-step convergence analysis. (**a**) Different mesh densities. (**b**) Different time-steps.

Then, the time-step convergence verification is undertaken. Similar to the mesh density convergence verification, the process of the glider entering water is calculated using three different time steps, which are 5×10^{-5} s, 2×10^{-5} s and 1×10^{-5} s. Figure 8b depicts the glider axial force variation over time. At a time-step of 5×10^{-5} s, the axial force change is the same as the results when the time-step is 1×10^{-5} s, but the peak value is slightly smaller. When the time-step is 2×10^{-5} s, the axial force time history is almost the same as the results when the time-step is 1×10^{-5} s. Considering the calculation efficiency and result accuracy, a time-step of 2×10^{-5} s is adopted in the subsequent calculation.

4. Results and Discussion

4.1. Influence of Wings on the Impact Load

Unlike AUVs with a slender body shape, the wing structure of an underwater glider adds complexity to its water entry impact load characteristics. In this section, water entry processes are simulated for an underwater glider with wings and an AUV without wings under identical water entry conditions by the same numerical method. The airdropped AUV model is obtained by deleting the appendages of the airdrop underwater glider, which makes it have the same shape as the main body of the airdrop underwater glider. We analyze how the glider impact load during water entry is affected by the wings. The water entry conditions include a 10 m/s velocity, a 90° entry angle and a 10°attack angle.

The time-dependent variations in radial and axial accelerations for the airdropped underwater glider and the AUV are shown in Figures 9 and 10, respectively. It should be pointed out that the absolute value of acceleration is used to measure its size, and the sign of acceleration is used to measure its direction. For example, when the axial acceleration is positive, it means that the direction of acceleration is the same as the positive direction of the O_0X_0 axis. When the axial acceleration is negative, it means that the direction of acceleration is the same as the negative direction of the O_0X_0 axis. In addition, because the positive O_0X_0 axis direction and the positive O_0Z_0 axis direction of the body coordinate frame are biased below the horizontal plane, the graphs are rotated with positive values down to maintain consistency with the body frame.

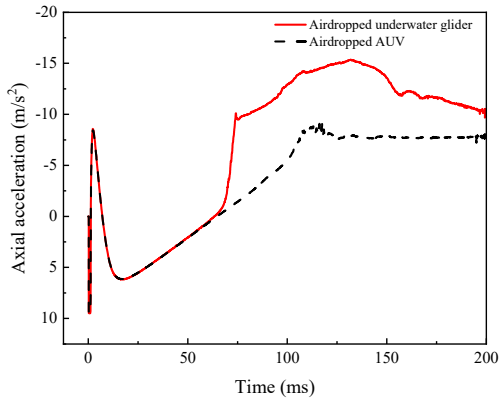

Figure 9. Time history of axial acceleration.

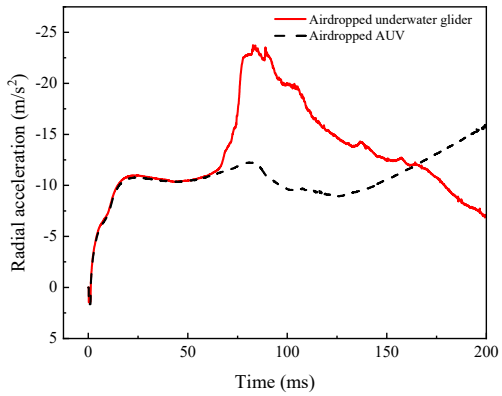

Figure 10. Time history of radial acceleration.

Before 60 ms, both the radial and axial accelerations of the glider are the same as those of the AUV. After 60 ms, the absolute values of the radial and axial accelerations both increase rapidly because of the impact load generated by the wings entering the water. Both the axial and radial accelerations are negative, which means that their directions are negative on the O_0X_0 axis and negative on the O_0Z_0 axis, respectively. The peak axial acceleration caused by the wing's entry equals that caused by the bow's entry. The peak radial acceleration induced by the wing's water entry is approximately twice that of the bow's water entry. Moreover, the presence of the wing elevates both the radial and axial loads for the glider in the water entry process. The air-launched AVU experiences a peak axial acceleration of approximately -9.17 m/s^2, compared to approximately -15.36 m/s^2 in the glider. The wings boost the absolute value of the peak axial acceleration by approximately 67.5%. Similarly, the peak radial acceleration of the AVU is approximately -12.21 m/s^2, and approximately -23.75 m/s^2 for the glider with wings. The absolute value of the peak radial acceleration of the glider is 1.945 times that of the AUV, which means that the wings amplify the peak radial load by about 94.5%. Overall, the influence of wings on the glider's water entry impact load primarily manifests after the wings contact water, leading to a notable increase in both the peak axial and radial acceleration, with a more pronounced rise in the peak radial acceleration.

4.2. Impact Load Characteristics of Airdropped Underwater Glider

During the airdrop process, parachutes are used to decelerate the underwater glider and ensure its structural safety. After descending to a certain height, the glider separates from the parachute for free fall. Recognizing that the deviation of the parachute's lifting point from the glider's O_0X_0 axis may induce an attack angle during descent, when studying the impact load characteristics of the airdropped underwater glider, this paper sets the water entry velocity and angle as 10 m/s and 90°, respectively, and the attack angle as 10°.

Figure 11 shows the time-varying process of the glider impact load during water entry. Figure 12 portrays the state of the glider entering the water at typical moments.

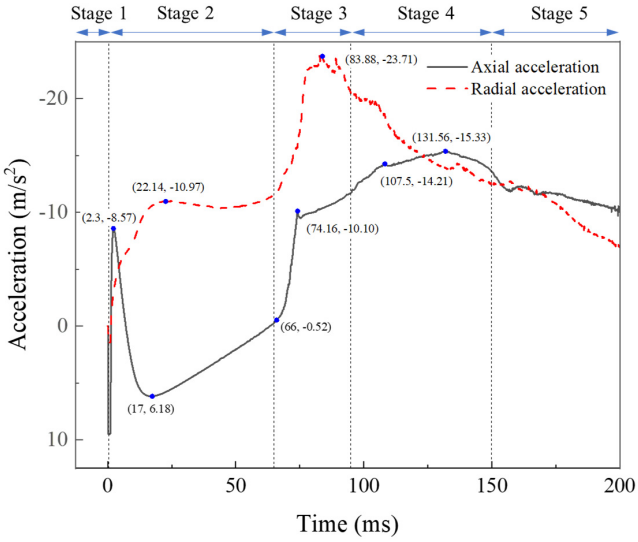

Figure 11. Time-varying process of the impact load of a glider entering the water.

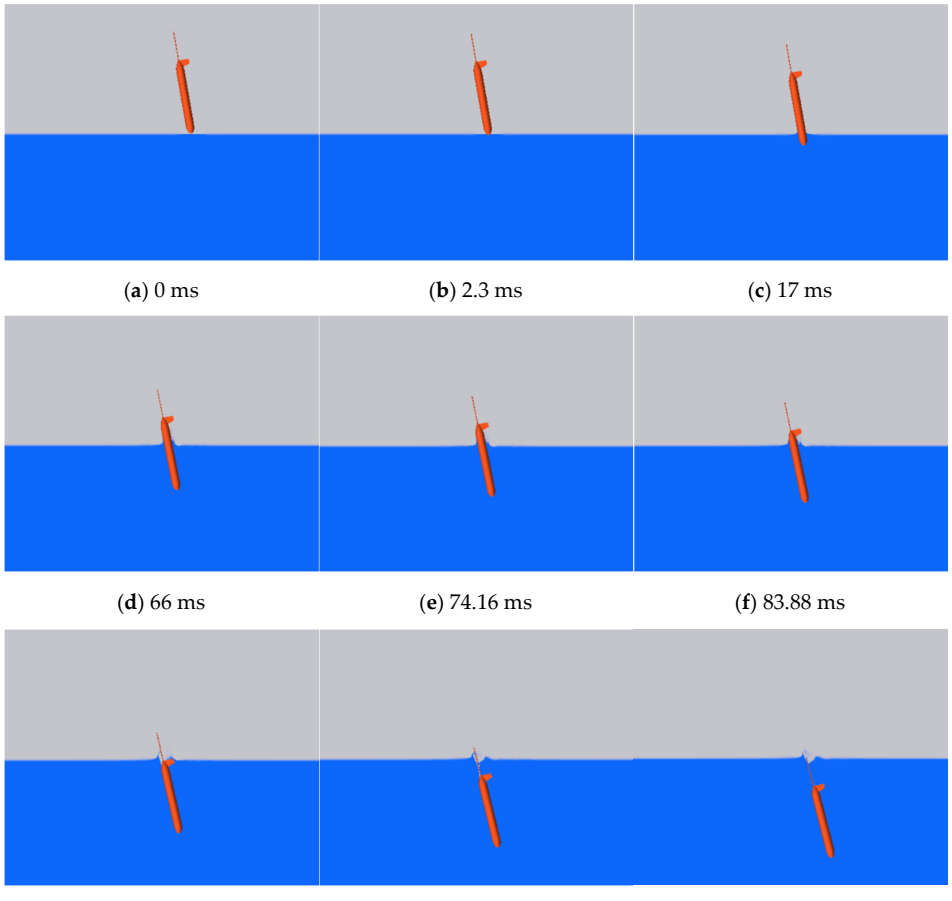

(**a**) 0 ms (**b**) 2.3 ms (**c**) 17 ms

(**d**) 66 ms (**e**) 74.16 ms (**f**) 83.88 ms

(**g**) 107.5 ms (**h**) 131.56 ms (**i**) 150 ms

Figure 12. The state of the glider entering the water at typical moments.

For an airdropped underwater glider, its water impact process can be divided into different stages according to the load change process. Combining the load change process

shown in Figure 11 and the water entry state depicted in Figure 12, the process of the glider entering water can be split into the five stages shown below:

Stage 1, Free-Fall Stage. The glider has not touched the water yet and remains in free fall. At this stage, the acceleration of the glider is 9.8 m/s^2, and the velocity is about 10 m/s.

Stage 2, Bow Entry Stage. From the moment the bow contacts water, the slamming pressure on the bow increases sharply. The axial acceleration of the glider changes rapidly and reaches its first peak at -8.57 m/s^2 at 2.3 ms. At this time, the slamming load of the glider is greater than the gravity, so the axial acceleration direction of the glider is the negative direction of the O_0X_0 axis. Due to the transient characteristics of the slamming pressure, the axial acceleration peaks and then drops rapidly. When the slamming load is less than gravity, the axial acceleration of the glider is in the same direction as the component of gravity on the O_0X_0 axis, which is the positive direction of the O_0X_0 axis. At 17 ms, the water resistance reaches the minimum value, and the axial acceleration of the glider is 6.18 m/s^2. As the immersion depth increases, the water resistance gradually increases, leading to a decrease in the glider axial acceleration. Meanwhile, the glider radial impact load increases rapidly from the moment the bow contacts water. With an increase in the immersion depth, the radial acceleration generated by water resistance gradually changes, reaching -10.97 m/s^2 at 22.14 ms. The direction of radial acceleration is the negative direction of the O_0Z_0 axis.

Stage 3, Wing Entry Stage. As the immersion depth further increases, the water resistance gradually becomes greater than gravity, causing the axial acceleration direction of the glider to be opposite to the direction of gravity, and it begins to increase. From the time when the wing contacts water, the glider axial acceleration changes rapidly again due to the slamming pressure of the wing. The second peak value (-10.10 m/s^2) of the axial acceleration occurs at 74.16 ms. At this time, the water resistance experienced by the glider is greater than gravity, coupled with the slamming force generated by the wings entering the water, resulting in a somewhat larger absolute value for the second axial acceleration peak compared to the corresponding first peak. During the descent of the wing slamming force, the glider's water resistance is enhanced significantly because of the water entry of the wings, so the absolute value of the glider's axial acceleration drops slightly and then begins to rise. At this stage, the axial acceleration direction of the glider is in the negative direction of the O_0X_0 axis. From the moment the wing touches the water, the absolute value of the glider's radial acceleration increases rapidly and reaches the peak radial acceleration at 83.88 ms. At this time, the radial acceleration of the glider is -23.71 m/s^2, and its direction is the negative direction of the O_0X_0 axis.

Stage 4, Tail Entry Stage. As the immersion depth continues to increase, the water resistance further increases, and the absolute value of the glider's axial acceleration rises gradually. Upon the entry of the tail into water at 107.5 ms, the third peak in the axial acceleration value occurs. At 131.56 ms, the absolute value of the glider's axial acceleration reaches its maximum value. At this time, the axial acceleration of the glider is -15.33 m/s^2, and its direction is the negative direction of the O_0X_0 axis. After that, the absolute value of acceleration begins to decrease gradually. The absolute value of the glider's radial acceleration continues to decrease throughout the Tail Entry Stage.

Stage 5, Full Immersion Stage. The glider is completely submerged in the water. The absolute value of the glider's acceleration decreases gradually.

In summary, the glider acceleration changes rapidly in Stages 2 and 3 during the water entry event. This suggests that the bow and wings bear greater impact loads during water entry, resulting in a higher risk of damage to the glider, which requires special attention.

4.3. Influence of Water Entry Angle on the Impact Load

If the underwater glider is significantly affected by wind speed prior to parachuting, its water entry angle may vary. This section explores how the water entry angle influences the glider impact load by simulating the process of glider entry into water at various entry angles (60°, 70°, 80°, and 90°). The attack angle and water entry velocity are set at 0° and

10 m/s, respectively. Figures 13 and 14 display the changes in the glider's axial acceleration and radial acceleration with time at various water entry angles, respectively.

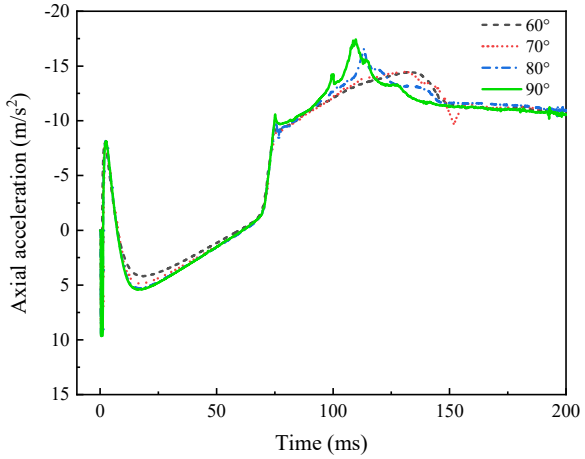

Figure 13. Time history of axial acceleration.

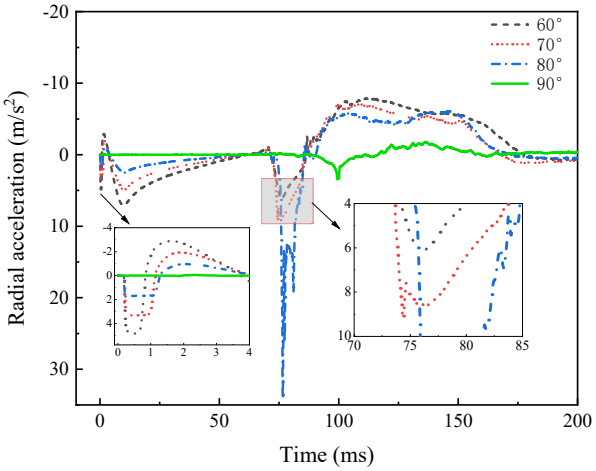

Figure 14. Time history of radial acceleration.

Figures 13 and 14 illustrate that during the Bow Entry Stage, the water entry angle exerts minimal influence over the glider peak axial acceleration, which remains approximately -8.15 m/s^2 across different entry angles. However, with a decrease in the angle, the peak radial acceleration progressively increases. Specifically, at 60°, the glider experiences a peak radial acceleration of 7.01 m/s^2. Figures 13 and 14 also illustrate that during the Wing Entry Stage, the absolute value of the glider's peak axial acceleration drops with the decrease in the water entry angle: the peak axial acceleration is -10.58 m/s^2 at 90° and -9.22 m/s^2 at 70°, and the peak radial acceleration at 60° is comparable to that at 70°. Additionally, the peak radial acceleration value initially increases and then decreases: it is nearly 0 at 90°, peaks at 34.02 m/s^2 at 80°, and at 60°, the peak radial acceleration is 6.15 m/s^2. It is worth noting that when the water entry angle is 80°, the radial acceleration fluctuates sharply after reaching its peak before starting to fall back. As the water entry angle gradually decreases, the fluctuation after the radial acceleration reaches its peak gradually disappears. When the water entry angle is 60°, the radial acceleration reaches its peak and gradually falls back, no longer fluctuating.

As is clear from Figure 14, the peak value of the glider radial acceleration rises first and then drops as the water entry angle decreases. To further explore the correlation of the peak radial acceleration with the water entry angle, this section calculates the peak value of the glider radial acceleration at more water entry angles, and Figure 15 displays

the relevant results. Clearly, starting from the vertical entry into the water, the peak radial acceleration of the glider gradually increases with the decrease in the water entry angle. It peaks at about 80°. With a further decrease in the angle, the glider radial acceleration also drops gradually.

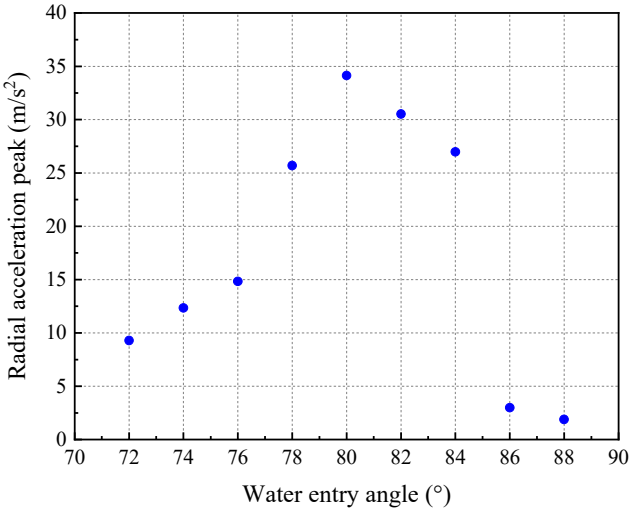

Figure 15. Variation in radial acceleration peak value with water entry angle.

The load acting on the wings will generate bending moments, and excessive moments may cause the wing to deform or even break. In this section, the wing root axis Line a and the wing trailing edge axis Line b, as shown in Figure 3, are selected to analyze the moment of the glider wing. Figure 16 shows the moment of the wing around Line a and Line b changing with time during the glider water entry. As is clear, both the moments around Line a and Line b change over time in a similar manner to the glider radial acceleration in Stage 3. In other words, if the glider radial acceleration is large, the moments of the wing around Line a and Line b are also large.

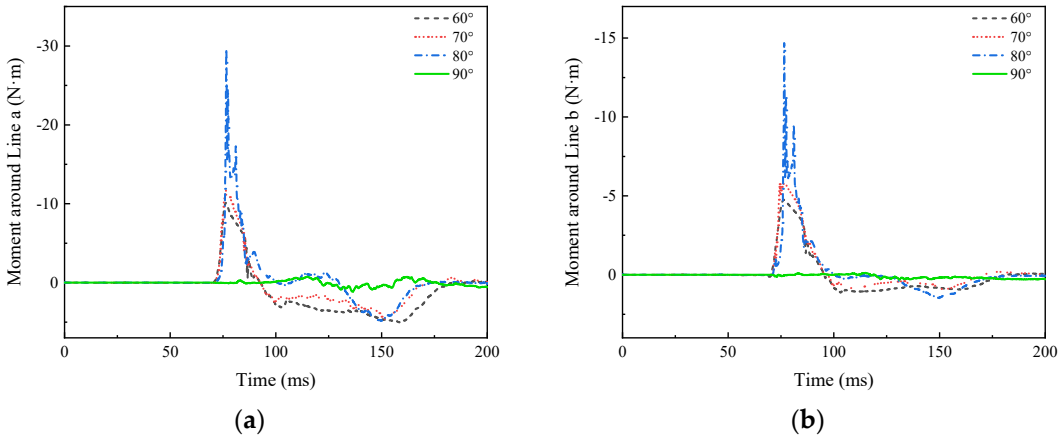

Figure 16. Wing moment with different water entry angles. (**a**) Moment around Line a. (**b**) Moment around Line b.

Analysing the glider impact load during water entry at various entry angles reveals how the impact load is affected by the water entry angle. This influence encompasses the following two aspects:

(1) During Bow Entry Stage, water entry angle exerts minimal influence over the peak axial acceleration, which remains approximately -8.15 m/s^2 across different entry angles. Conversely, the peak radial acceleration increases as the water entry angle decreases, being nearly 0 at a 90° water entry angle, reaching about 7.01 m/s^2 at a 60° water entry angle.

(2) During Wing Entry Stage, the absolute value of the glider's peak axial acceleration decreases slightly as the water entry angle decreases: at 90°, the peak axial acceleration is −10.58 m/s^2, while at 60°, it is −9.22 m/s^2; this absolute value decreases by approximately 12.8% in contrast to that at 90°. Furthermore, the peak radial acceleration initially increases then decreases with decreasing entry angle: at 90°, the peak radial acceleration is nearly 0 m/s^2, reaching a maximum of 34.02 m/s^2 at 80°, and decreasing to 6.15 m/s^2 at 60°, which is approximately 81.9% lower than at 80°. The variation in the wing moment mirrors that of the radial acceleration.

4.4. Influence of Attack Angle on the Impact Load

The glider may experience a specific attack angle during descent due to the parachute's lifting position. This section simulates the process of the glider entering water at various attack angles (0°, 10°, 20°, and 30°) to examine its influence on the impact load. The water entry velocity and angle are set to 10 m/s and 90°, respectively. Figures 17 and 18 display the changes in the glider's axial and radial accelerations with time at various attack angles, respectively.

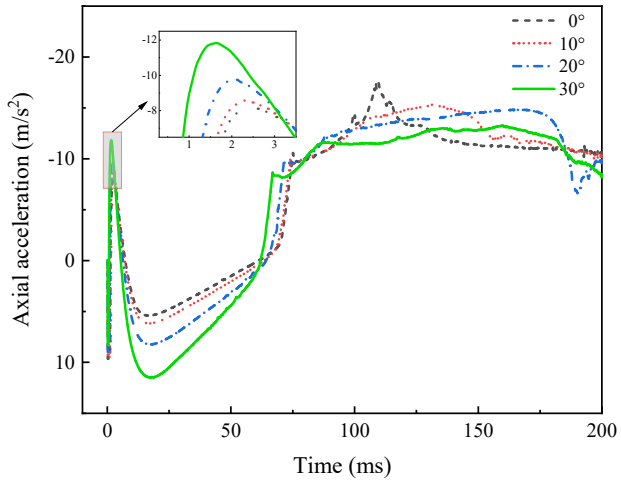

Figure 17. Time history of axial acceleration.

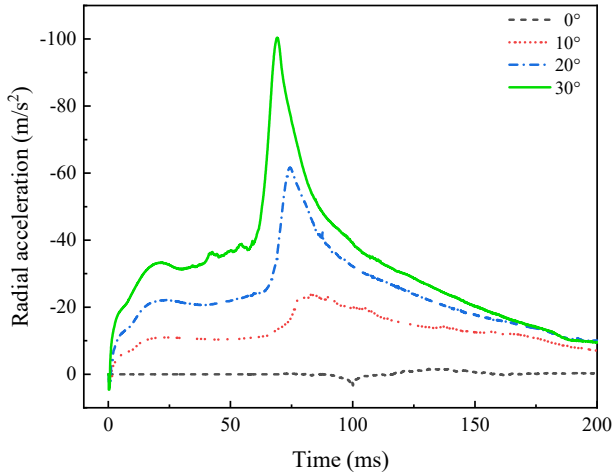

Figure 18. Time history of radial acceleration.

Figures 17 and 18 illustrate that during the Bow Entry Stage, the absolute value of the glider's peak axial acceleration increases as the attack angle gradually increases: at an attack angle of 10°, the peak axial acceleration is approximately −8.14 m/s^2; at 30°, it is about −11.83 m/s^2. Similarly, the absolute value of the glider's peak radial acceleration

also increases with the attack angle: at 10°, it is approximately −6.29 m/s^2; at 30°, it is about −33.27 m/s^2. Figures 17 and 18 also illustrate that during the Wing Entry Stage, the absolute value of the glider's peak axial acceleration declines with the gradual enlargement of the attack angle: at a 10° attack angle, the peak axial acceleration is −10.1 m/s^2, and at 30°, it is −8.65 m/s^2. Conversely, the absolute value of the glider's peak radial acceleration value substantially increases with the enlargement of the attack angle: at 10°, the peak radial acceleration is about −22 m/s^2, whereas at 30°, it is about −100 m/s^2.

Figure 19 shows the moment of the wing around the wing root and the wing trailing edge changing with time as the glider enters the water. As is clear, the glider wing moment increases as the attack angle enlarges. For every 10° increase in the attack angle, the peak wing moment almost doubles. The moment of the wing around the wing root axis Line a is greater than the moment around the wing trailing edge axis Line b. When the attack angle is 30°, the moment around Line a is about 60 N·m, and the moment around Line b is about 20 N·m. Additionally, the moments around Line a and Line b change over time in a similar manner to the glider radial acceleration in Stage 3.

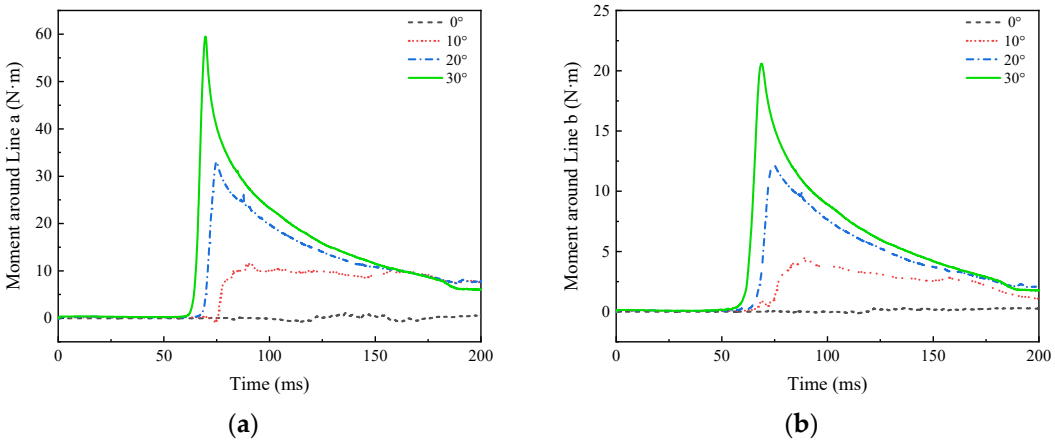

Figure 19. Wing moment with different attack angles. (**a**) Moment around Line a. (**b**) Moment around Line b.

Analyzing the glider impact load during water entry at various attack angles reveals how the impact load is affected by the attack angle. This influence encompasses the following two aspects:

(1) Bow Entry Stage. As the attack angle increases, the absolute value of the glider's peak axial acceleration gradually rises: at a 10° attack angle, the peak axial acceleration measures approximately −8.14 m/s^2, whereas at 30°, it is about −11.83 m/s^2, marking a 45.3% increase in the absolute value compared to 10°. Similarly, the absolute value of the peak radial acceleration exhibits a significant increase: at a 10° attack angle, it is around −6.29 m/s^2, while at 30°, it is about −33.27 m/s^2; the absolute value is approximately 4.29 times higher than at 10°.

(2) Wing Entry Stage. With the gradual increase in the attack angle, the absolute value of the glider's peak axial acceleration decreases: at a 10° attack angle, it is about −10.1 m/s^2, while at 30°, it is approximately −8.65 m/s^2, marking a 14.3% decrease in the absolute value compared to 10°. Conversely, the absolute value of the peak radial acceleration of the glider exhibits a significant increase: at a 10° attack angle, it is approximately −22 m/s^2, whereas at 30°, it is about −100 m/s^2; the absolute value is roughly 4.55 times higher than at 10°. The variation in the wing moment correlates with the radial acceleration.

4.5. Influence of Water Entry Velocity on the Impact Load

Accurately controlling the height when the glider separates from the parachute is challenging, impacting the glider's water entry velocity. Therefore, this section conducts numerical simulations on the process of the glider entering into water at various entry

velocities (10 m/s, 20 m/s and 30 m/s) to examine how the glider impact load is affected by the water entry velocity. Figures 19 and 20 display the changes in the glider's axial and radial accelerations with time at various water entry velocities, respectively, under a 90° water entry angle and a 30° attack angle.

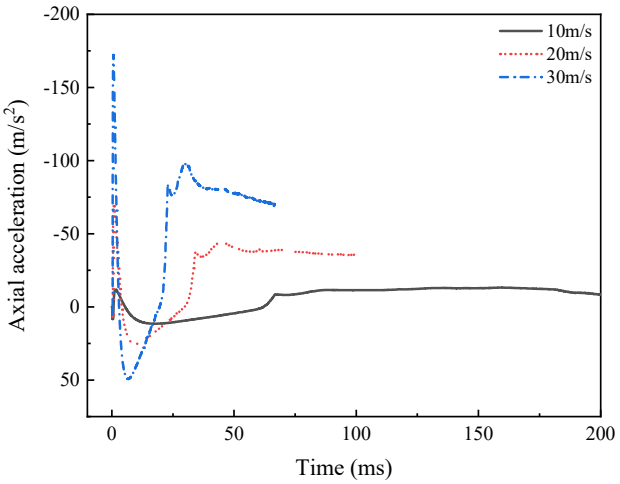

Figure 20. Time history of axial acceleration.

Figures 20 and 21 illustrate that with an increase in the water entry velocity, the duration of each stage of the glider's water entry decreases, and the peak acceleration significantly rises. However, despite the changes in impact load, the stages remain distinguishable. The impact load versus time curves at different water entry velocities exhibit some similarities. In order to compare the similarities of impact loads under different water entry velocities, we scaled the curves based on the data at the initial velocity V_1 = 10 m/s. The scaling ratio of time is relative to velocity, so that the glider has the same relative time in the water entry process at different water entry velocities. The scaling ratio of water entry impact loads is the square of the water entry relative velocity, so that the glider has similar relative impact loads in the water entry process at different water entry velocities. The time and impact loads are scaled by Equation (4), and the variation in the relative load with relative time is depicted in Figures 22 and 23. The variation in the relative load with relative time is remarkably similar across various water entry velocities. Thus, we can infer that the impact load is directly proportional to the square of impact velocity, while the duration of the impact process is inversely proportional to the impact velocity. Importantly, at a 20 m/s impact velocity, the variation in the relative load with relative time aligns more closely with that of the 30 m/s impact velocity, but differs somewhat from that of the 10 m/s impact velocity. This is due to the omission of the effect of gravity in Equation (4). At a 10 m/s impact velocity, the impact load is relatively small, with gravity exerting a significant influence on the relative results. However, when the impact velocity exceeds 20 m/s, the impact load becomes relatively large, with gravity contributing minimally to the relative results.

$$\begin{aligned} Rt &= t \times \frac{V_i}{V_1}, \quad i = 1,\ 2,\ 3 \\ Ra &= a \times \left(\frac{V_1}{V_i}\right)^2, \quad i = 1,\ 2,\ 3 \\ RM &= M \times \left(\frac{V_1}{V_i}\right)^2, \quad i = 1,\ 2,\ 3 \end{aligned} \tag{4}$$

where t is time, and Rt is the relative time; a is acceleration, and Ra is the relative acceleration; M is the moment, and RM is the relative moment; and V_i is the water entry velocity, V_1 = 10 m/s, V_2 = 20 m/s, and V_3 = 30 m/s.

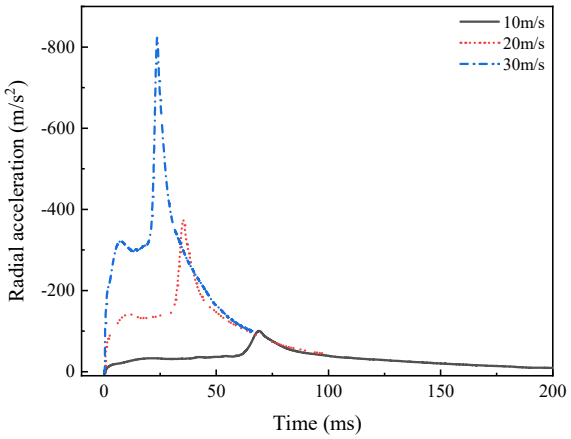

Figure 21. Time history of radial acceleration.

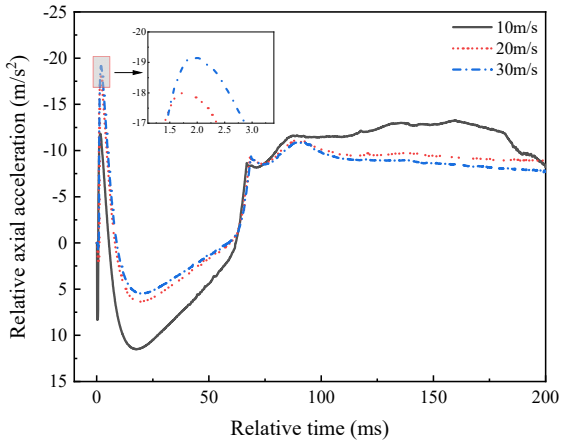

Figure 22. Time history of relative axial acceleration.

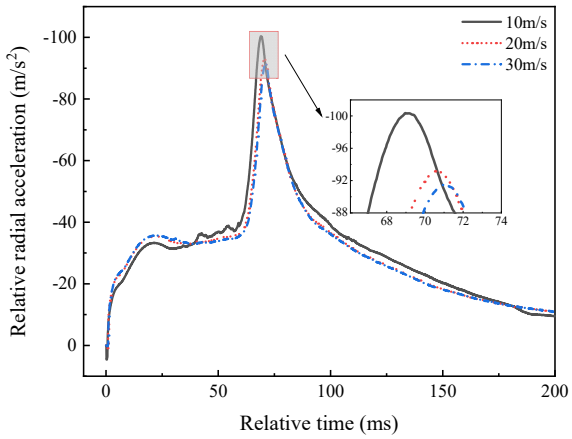

Figure 23. Time history of relative radial acceleration.

Figure 24 depicts the variation in the wing moment around the wing root and the wing trailing edge with time during the glider's water entry. Similar to the impact load, the time curves for the wing moment at various water entry velocities exhibit resemblance. The curves of the wing moments around Line a and Line b show similar trends with time under different impact velocities. The wing moment is also scaled according to Equation (4), as depicted in Figure 25. Noticeably, the wing moment has the same relationship with the impact velocity as the glider impact load. When the velocity exceeds 20 m/s, the relative

wing moment is directly proportional to the square of the impact velocity, while the impact process duration is inversely proportional to the impact velocity.

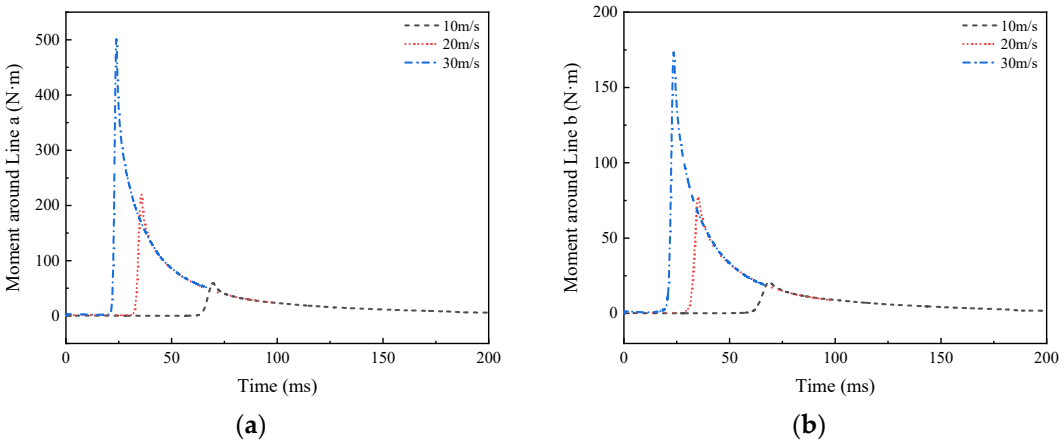

Figure 24. Wing moment with different water entry velocities. (**a**) Moment around Line a. (**b**) Moment around Line b.

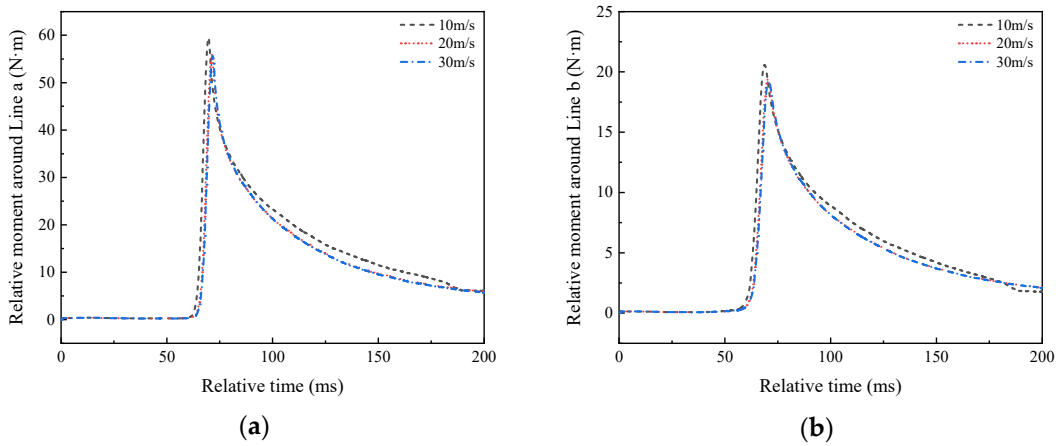

Figure 25. Relative wing moment with different water entry velocities. (**a**) Relative moment around Line a. (**b**) Relative moment around Line b.

Generally, the glider's axial acceleration, radial acceleration, and wing moment increase proportionally with the square of the entry speed. When scaled by the square of the entry speed, the slamming loads at different speeds are essentially equivalent.

5. Conclusions

This paper utilizes the CFD method to analyze the impact load characteristics of airdropped underwater gliders during entry into water. The glider water entry process is divided into distinct stages, allowing for an in-depth exploration of the load characteristics at each stage. Furthermore, the research explores the influences of the entry angle, velocity and attack angle on both the bow and wing impact loads. The outcomes of this study afford valuable insights into the structural design and control of water entry strategies for airdropped underwater gliders. The major conclusions reached are as follows:

(1) The influence of the wings on the glider impact load during water entry becomes significant once the wing enters into water. During this phase, there is a notable increase in both the absolute value of the glider's peak axial and radial acceleration, with the radial acceleration experiencing a more pronounced enhancement.

(2) Depending on the variation in the impact load, the process of the glider entering water can be split into the Free-Fall Stage, Bow Entry Stage, Wing Entry Stage, Tail Entry

Stage, and Full Immersion Stage. The Bow Entry Stage and Wing Entry Stage, in particular, demonstrate notable peaks in both the axial and radial acceleration, which deserve careful consideration.

(3) The water entry angle has the most significant impact on the peak radial acceleration of the glider during the wing entry stage. As the water entry angle gradually decreases, the peak radial acceleration initially increases and then decreases, reaching a maximum value of 34.02 m/s^2 at an 80° water entry angle.

(4) The attack angle has the most significant impact on the glider's peak radial acceleration. As the attack angle gradually increases, the absolute value of the glider's peak acceleration also increases. When the attack angle is 30°, the peak radial acceleration of the glider during the bow entry stage is -33.27 m/s^2, its direction is the negative direction of the O_0Z_0 axis, and its absolute value is approximately 5.29 times that at a 10° attack angle. Similarly, the peak radial acceleration is -100.36 m/s^2, its direction is the negative direction of the O_0Z_0 axis, and its absolute value is about 4.46 times that at a 10° attack angle.

(5) The axial acceleration and radial acceleration exhibit a direct proportionality to the square of the water entry velocities, which is consistent with the water slamming load characteristics of the AUV [16]. Furthermore, the wing moments also exhibit a direct proportionality to the square of the water entry velocities.

Future works will take the influence of hydroelasticity into account in the load calculations to more accurately reflect the impact loads during the entry of airdropped underwater gliders into water.

Author Contributions: Conceptualization, X.W. and L.W.; methodology, X.W. and L.W.; software, X.W. and L.W.; validation, P.Y., X.C. and L.W.; formal analysis, X.W. and L.W.; investigation, P.Y., X.W. and L.W.; resources, X.W. and L.W.; data curation, P.Y., X.W. and L.W.; writing—original draft preparation, X.W. and L.W.; writing—review and editing, L.W. and P.Y.; visualization, X.W. and L.W.; supervision, X.W., P.Y. and L.W.; project administration, X.W., P.Y. and L.W.; funding acquisition, P.Y. and L.W. All authors have read and agreed to the published version of the manuscript.

Funding: This work was supported by the National Key Research and Development Program of China [2021YFC2801102]; Joint Fund of Science & Technology Department of Liaoning Province, State Key Laboratory of Robotics [2023-O15]; Key-Area Research and Development Program of Guangdong Province [2020B1111010004] and Shanghai Ship Engineering Key Laboratory Fund (Grant Nos. SE202301).

Institutional Review Board Statement: Not applicable.

Informed Consent Statement: Not applicable.

Data Availability Statement: The original contributions presented in the study are included in the article.

Conflicts of Interest: The authors declare no conflicts of interest.

References

1. Wu, Q.; Wu, H.; Jiang, Z.; Tan, L.; Yang, Y.; Yan, S. Multi-objective optimization and driving mechanism design for controllable wings of underwater gliders. *Ocean. Eng.* **2023**, *286*, 115534. [CrossRef]
2. Karman, T.V. *The Impact of Seaplane Floats during Landing*; Technical Report Archive & Image Library: Aachen, Germany, 1929.
3. Wagner, H. Phenomena Associated with Impacts and Sliding on Liquid Surfaces. *J. Appl. Math. Mech.* **1932**, *12*, 193–215.
4. Miloh, T. On the initial-stage slamming of a rigid sphere in a vertical water entry. *Appl. Ocean Res.* **1991**, *13*, 43–48. [CrossRef]
5. Korobkin, A. Analytical models of water impact. *Eur. J. Appl. Math.* **2004**, *15*, 821–838. [CrossRef]
6. Aquelet, N.; Souli, M.; Olovsson, L. Euler-Lagrange coupling with damping effects: Application to slamming problems. *Comput. Methods Appl. Mech. Eng.* **2006**, *195*, 110–132. [CrossRef]
7. Wang, S.; Soares, C.G. Numerical study on the water impact of 3D bodies by an explicit finite element method. *Ocean Eng.* **2014**, *78*, 73–88. [CrossRef]
8. Panciroli, R.; Abrate, S.; Minak, G.; Zucchelli, A. Hydroelasticity in water-entry problems: Comparison between experimental and SPH results. *Compos. Struct.* **2012**, *94*, 532–539. [CrossRef]
9. Facci, A.L.; Porfiri, M.; Ubertini, S. Three-dimensional water entry of a solid body: A computational study. *J. Fluids Struct.* **2016**, *66*, 36–53. [CrossRef]

10. Bilandi, R.N.; Jamei, S.; Roshan, F.; Azizi, M. Numerical simulation of vertical water impact of asymmetric wedges by using a finite volume method combined with a volume-of-fluid technique. *Ocean Eng.* **2018**, *160*, 119–131. [CrossRef]
11. Yu, P.; Zhang, B.; Yang, Z.; Wang, T. Numerical Investigation on the Shallow Water Entry of Wedges. *IEEE Access* **2019**, *7*, 170062–170076. [CrossRef]
12. Wang, Q.; Zhang, B.R.; Yu, P.Y.; Li, G.Z.; Yuan, Z.J. Numerical Investigation on the Water Entry of Several Different Bow-Flared Sections. *Appl. Sci.* **2020**, *10*, 7952. [CrossRef]
13. Xie, H.; Liu, F.; Liu, X.; Tang, H. Numerical prediction of asymmetrical ship slamming loads based on a hybrid two-step method. *Ocean Eng.* **2020**, *208*, 107331. [CrossRef]
14. Yan, G.-X.; Pan, G.; Shi, Y.; Chao, L.-M.; Zhang, D. Experimental and numerical investigation of water impact on air-launched AUVs. *Ocean Eng.* **2018**, *167*, 156–168. [CrossRef]
15. Chaudhry, A.Z.; Shi, Y.; Pan, G.; Liu, G. Mechanical characterization of flat faced deformable AUV during water entry impact considering the hydroelastic effects. *Appl. Ocean Res.* **2021**, *115*, 102849. [CrossRef]
16. Shi, Y.; Pan, G.; Yan, G.X.; Yim, S.C.; Jiang, J. Numerical study on the cavity characteristics and impact loads of AUV water entry. *Appl. Ocean Res.* **2019**, *89*, 44–58. [CrossRef]
17. Shi, Y.; Pan, G.; Yim, S.C.; Yan, G.; Zhang, D. Numerical investigation of hydroelastic water-entry impact dynamics of AUVs. *J. Fluids Struct.* **2019**, *91*, 102760. [CrossRef]
18. Wang, X.H.; Shi, Y.; Pan, G.; Chen, X.; Zhao, H.R. Numerical research on the high-speed water entry trajectories of AUVs with asymmetric nose shapes. *Ocean Eng.* **2021**, *234*, 15. [CrossRef]
19. Chen, X.; Bose, N.; Brito, M.; Khan, F.; Thanyamanta, B.; Zou, T. A Review of Risk Analysis Research for the Operations of Autonomous Underwater Vehicles. *Reliab. Eng. Syst. Saf.* **2021**, *216*, 108011. [CrossRef]
20. Pelland, N.A.; Eriksen, C.C.; Lee, C.M. Subthermocline eddies over the Washington continental slope as observed by Seagliders. *J. Phys. Oceanogr.* **2003**, *43*, 2025–2053. [CrossRef]
21. Hristova, H.G.; Kessler, W.S.; McWilliams, J.C.; Molemaker, M.J. Mesoscale variability and its seasonality in the Solomon and Coral Seas. *J. Geophys. Res. Ocean.* **2014**, *119*, 4669–4687. [CrossRef]
22. Wu, X.C.; Chang, X.; Liu, S.W.; Yu, P.Y.; Zhou, L.L.; Tian, W. Numerical Study on the Water Entry Impact Forces of an Airdropped underwater glider under Wave Conditions. *Shock Vib.* **2022**, *8*, 116506.
23. Shang, Y.C.; Horrillo, J.J. Numerical Simulation and Hydrodynamic Performance Predicting of 2 Two-Dimensional Hydrofoils in Tandem Configuration. *J. Mar. Sci. Eng.* **2021**, *9*, 462. [CrossRef]
24. Piskur, P. Strouhal Number Measurement for Novel Biomimetic Folding Fins Using an Image Processing Method. *J. Mar. Sci. Eng.* **2022**, *10*, 484. [CrossRef]
25. Chen, C.W.; Lu, Y.F. Computational Fluid Dynamics Study of Water Entry Impact Forces of an Airborne-Launched, Axisymmetric, Disk-Type Autonomous Underwater Hovering Vehicle. *Symmetry* **2019**, *11*, 1100. [CrossRef]
26. Shen, C.; Yu, P.Y.; Wang, T.L.; Chen, N.Z. A CFD based Kriging model for predicting the impact force on the sphere bottom during the early-water entry. *Ocean Eng.* **2022**, *243*, 110304. [CrossRef]
27. Aristoff, J.M.; Truscott, T.T.; Techet, A.H.; Bush, J.W.M. The water entry of decelerating spheres. *Phys. Fluids* **2010**, *22*, 032102. [CrossRef]